

¹ **Effect of local host density and size forest insect severity depends
2 on climatic water deficit**

³ Michael J. Koontz^{1,2,*}, Andrew M. Latimer^{1,2}, Leif A. Mortenson³, Christopher J. Fettig³, Constance I.
⁴ Millar⁴, Malcolm P. North^{1,2,5}

⁵ ¹Graduate Group in Ecology, University of California, Davis, CA, USA

⁶ ²Department of Plant Sciences, University of California, Davis, CA, USA

⁷ ³USDA Forest Service, Pacific Southwest Research Station, Placerville, CA, USA

⁸ ⁴USDA Forest Service, Pacific Southwest Research Station, Albany, CA, USA

⁹ ⁵USDA Forest Service, Pacific Southwest Research Station, Davis, CA, USA

¹⁰ *Correspondence: michael.koontz@colorado.edu

¹¹ Date report generated: April 01, 2019

¹² **Abstract**

¹³ Bark beetles are a primary mortality agent of trees in western U.S. forests, and the recent Californian hot
¹⁴ drought of 2012 to 2015 created favorable conditions for bark beetle-induced tree mortality throughout the
¹⁵ yellow pine/mixed-conifer forest system in the Sierra Nevada mountain range. The western pine beetle,
¹⁶ *Dendroctonus brevicomis*, is the forest insect that is largely responsible for the especially common deaths of its
¹⁷ main host in California, the ponderosa pine tree (*Pinus ponderosa*). While previous work has demonstrated a
¹⁸ link between climate conditions related to tree water stress and forest density on the severity of the western
¹⁹ pine beetle disturbance, it remains challenging to disentangle the relative effects of these variables. Further,
²⁰ forest density can affect western pine beetle behavior in a number of ways, which creates a need for more
²¹ information on complex forest structure (including local density, tree size, and the heterogeneity of these
²² variables across a forest stand) to uncover the most likely mechanism.

²³ We conducted aerial surveys over an established network of 32 permanent vegetation monitoring plots along
²⁴ a 350km and 1000m elevation gradient in the Sierra Nevada mountain range of California using a small,
²⁵ unhumanned aerial system (sUAS aka drone) equipped with a narrow-band multispectral camera. Using
²⁶ Structure from Motion (SfM) processing on over 450,000 images, we reconstructed the complex vegetation
²⁷ structure of over 9 square kilometers of forest that experienced ponderosa pine mortality as a result of
²⁸ western pine beetle activity. Using this dataset, we built a model to predict the probability of ponderosa
²⁹ pine mortality as a function of forest structure variables (including ponderosa pine density and mean size, as

30 well as all tree density and mean size), an environmental gradient of climatic water deficit, and a Gaussian
31 process to capture spatial covariance in the response. We found that host tree

32 Data from small, unhummaned aerial systems (sUAS) can provide important context surrounding ground
33 plots, which enables inference and generates new insights into ecological processes. sUAS are best-suited to
34 enhancing ground data, which implies that we need not abandon lessons learned from sound experimental
35 design (i.e., a network of plots along a gradient is still a powerful way to use sUAS data).

36 Host availability for aggressive bark beetles appears to have played the dominant role in increasing the probability
37 of ponderosa pine mortality in the most hard-hit forest stands during the cumulative mortality event of 2012 to 2018. Host size played a role in its interaction with environmental condition— climatic water
38 deficit— such that smaller trees increased the probability of ponderosa mortality at cool/wet sites, while larger
40 trees increased the probability of ponderosa mortality at hot/dry sites.

41 Introduction

42 Aggressive bark beetles dealt the final blow to many of the nearly 150 million trees killed in the California
43 drought of 2012 to 2015 and its aftermath (USDAFS 2019). A harbinger of climate change effects to come,
44 high temperatures exacerbating the extreme drought led to tree mortality events of unprecedented size in the
45 driest, densest forests across the state (Millar and Stephenson 2015, Young et al. 2017). A century of fire
46 suppression policy has enabled forests to grow into dense stands, which increases water stress on trees and
47 makes them more vulnerable to bark beetle attack (Fettig 2012, North et al. 2015).

48 Forests in California’s Sierra Nevada region are characterized by regular bark beetle disturbances that interact
49 with forest structure. Bark beetles shape forest structure as they sporadically kill weakened trees under
50 normal conditions, or wide swaths of even healthy trees under outbreak conditions (Raffa et al. 2015). Forest
51 structure also strongly influences bark beetle activity. Low-density forests are less prone to bark beetle
52 attacks (Fettig 2012), but resolving the mechanism underlying this observation requires a more nuanced view
53 of forest structure. For instance, a low-density forest may resist attack because longer dispersal distances are
54 required for successful colonization of new hosts, because widely-spaced trees experience less competition
55 for water resources and thus average tree vigor is greater (Hayes et al. 2009), or because its wider canopy
56 openings disrupt pheromone signaling between beetles (Fettig 2012).

57 Density is often a coarse gauge of the size and spatial distribution of trees— the forest structure— with which
58 bark beetles interact (Raffa et al. 2008). Climate change mitigation strategies emphasize reducing tree
59 densities (North et al. 2015, Young et al. 2017), but understanding the optimal scale and pattern of tree

60 distribution that can mitigate bark beetle outbreaks will be vital for predicting how California forests may
61 respond to these interventions. Recent research has shown a strong link between complex forest structure
62 and forest resilience, but measuring this complexity generally requires expensive equipment or labor-intensive
63 field surveys (Larson and Churchill 2012, Kane et al. 2014). These barriers restrict survey frequency and
64 extent, which limits insights into phenomena like bark beetle outbreaks that rapidly emerge over weeks to
65 months but have long-lasting effects on forest conditions. Further, the vast spatial extent and environmental
66 gradient of mortality (Young et al. 2017, USDAFS 2019) challenges our ability to simultaneously consider
67 how environmental conditions may interact with local forest structure to produce patterns of insect activity.
68 Small, unhumanned aerial systems (sUAS) enable fast and relatively cheap remote imaging over dozens of
69 hectares of forest, which can be used to determine both forest structure and tree condition at the individual
70 tree scale (Morris et al. 2017).

71 We used ultra-high resolution remote sensing data from a small, unhumanned aerial system over a network of
72 32 sites in the Sierra Nevada spanning 1000m of elevation and 350km of latitude and covering a total of 9
73 square kilometers of forest to ask how fine-scale forest structure affected the probability of tree mortality
74 during the cumulative mortality event of 2012 to 2018. We asked:

- 75 1. How does local host tree density and size affect the severity of western pine beetle disturbance?
- 76 2. How does total tree density and size affect the severity of western pine beetle disturbance?
- 77 3. How does environmentally-driven tree moisture stress affect the severity of western pine beetle distur-
78 bance?
- 79 4. Do the effects of forest structure and environmental condition on western pine beetle disturbance
80 interact?

81 Methods

82 Study system

83 The study sites comprise mostly ponderosa pine trees, *Pinus ponderosa*, whose primary bark beetle predator
84 in California is the western pine beetle (WPB), *Dendroctonus brevicomis*. The WPB is an aggressive bark
85 beetle, meaning it must attack and kill live trees in order to successfully reproduce (Raffa et al. 2008).
86 Pioneer WPBs disperse to a new host tree, determine the host's susceptibility to attack, and use pheromone
87 signals to attract other WPBs. The attracted WPBs mass attack the tree by boring into its inner bark,
88 laying eggs, and dying, leaving their offspring to develop inside the doomed tree before themselves dispersing
89 (Raffa et al. 2008). Small WPB populations prefer weakened trees but large populations can overwhelm

90 the defense mechanisms of even healthy trees. Successful attacks on large, healthy trees are boons to bark
91 beetle fecundity and trigger outbreaks in which populations explode and massive tree mortality occurs. In
92 California, the WPB can have 3 generations in a single year giving it a greater potential to spread rapidly
93 through forests than its more infamous congener, the mountain pine beetle, *Dendroctonus ponderosa* (MPB).

94 We built our study on 180 vegetation monitoring plots at 36 sites established between 2016 and 2017 (Fettig
95 et al. 2019). These established plots are located in beetle-attacked, mixed-conifer forests across the Eldorado,
96 Stanislaus, Sierra and Sequoia National Forests across an elevation gradient (3000-4000 feet, 4000-5000 feet,
97 and 5000+ feet above sea level) and have variable forest structure and disturbance history. Plot locations
98 were selected specifically in areas with >40% ponderosa pine basal area and >10% ponderosa pine mortality.
99 The 0.04ha circular plots are clustered along transects in groups of 5, with between 80 and 200m between
100 each plot. All trees within the plot were assessed as dead or alive. The stem location of all trees was mapped
101 relative to the center of each plot using azimuth/distance measurements. Tree identity to species and diameter
102 at breast height (dbh) were recorded if dbh was greater than 6.35cm. During the spring and early summer of
103 2018, all field plots were revisited to assess whether dead trees had fallen.

104 **Instrumentation**

105 Imagery was captured using a DJI Zenmuse X3 RGB camera (DJI 2015a) and a Micasense RedEdge3 5-band
106 multispectral camera (Micasense 2015). We mounted both of these instruments simultaneously on a DJI
107 Matrice 100 aircraft (DJI 2015b) using the DJI 3-axis stabilized gimbal for the Zenmuse X3 camera and a
108 Micasense angled fixed mount for the RedEdge3 camera. The gimbal and the angled fixed mount ensured
109 both instruments were nadir-facing during image capture. Just prior or after image capture at each site, we
110 calibrated the RedEdge3 camera by taking an image of a calibration panel on the ground in full sun with
111 known reflectance values for each of the 5 narrow bands.

Table 1: Reflectance sensitivity of the Micasense Rededge3 camera. The calibration panel value represents the reflectance of the calibration panel for the given wavelength.

Band number	Band name	Center wavelength	Band width	Wavelength range	Panel reflectance
1	blue (b)	475	20	465-485	0.64
2	green (g)	560	20	550-570	0.64
3	red (r)	668	10	663-673	0.64
4	near infrared (nir)	840	40	820-860	0.60

Band number	Band name	Center wavelength	Band width	Wavelength range	Panel reflectance
5	red edge (re)	717	10	712-722	0.63

112 **Flight protocol**

113 Image capture was conducted as close to solar noon as possible to minimize shadow effects (always within 4
 114 hours; usually within 2 hours). Prior to the aerial survey, two strips of bright orange drop cloth (~100cm x
 115 15cm) were positioned as an “X” over the permanent monuments marking the center of the 5 field plots from
 116 Fettig et al. (2019).

117 For each of the 36 sites (containing 5 plots each), we captured imagery over the surrounding ~40 hectares
 118 of forested area using north-south aerial transects. For XXXXX sites, we surveyed less surrounding area
 119 in order to maintain visual and radio communication with the aircraft during flight (Table XXXXXX; as a
 120 supplement, I think; Columns: Site, forest, elevation, rep, CWD, surveyed area, survey date).

121 We preprogrammed transect paths using Map Pilot for DJI on iOS (hereafter Map Pilot) (Easy 2018). All
 122 transects tracked the terrain and their altitude remained approximately constant at 120 meters above ground
 123 level in order to maintain consistent ground sampling distance in the imagery. Ground level was based on a
 124 1-arc-second digital elevation model (Farr et al. 2007) and we implemented terrain following using Map Pilot.
 125 For this analysis, we dropped 4 sites whose imagery was of insufficient quality to process.

126 Structure from motion (SfM) processing requires highly overlapping images, especially in densely vegetated
 127 areas. We planned transects with 90% forward overlap and 90% side overlap at 100 meters below the lens.
 128 Thus, with flights being at 120 meters above ground level, we achieved slightly higher than 90/90 overlap for
 129 objects 20 meters tall or shorter (91.6/91.6 overlap at the ground). Overlap values were based on focal length
 130 (3.6mm), sensor width (6.2mm), and image dimension (4000x3000 pixels) parameters of the Zenmuse X3
 131 camera. Images were captured at a constant rate of 1 image every 2 seconds for both cameras. A forward
 132 overlap of 90% at 100 meters translates to a flight speed of approximately 6.45 m/s and a side overlap of 90%
 133 at 100 meters translates to transects approximately 17.2 meters apart. The Rededge camera has a different
 134 focal length (5.4mm), sensor width (4.8mm), and image dimension (1280x960 pixels), which translates to
 135 image overlap of 80.7/80.7 at 100m below the lens and 83.9/83.9 at ground level. Approximately 1900 photos
 136 were captured over each 40 hectare survey area for each camera.

¹³⁷ **Structure from motion/Photogrammetric processing**

¹³⁸ We used structure from motion (SfM), aka photogrammetry, to generate orthorectified reflectance maps,
¹³⁹ digital surface models, and dense point clouds for each field site. We used Pix4Dmapper Cloud to process
¹⁴⁰ imagery using parameters ideal for images of a densely vegetated area taken by a multispectral camera.
¹⁴¹ For three sites, we processed the RGB and the multispectral imagery in the same project to enhance the
¹⁴² resolution of the dense point cloud. All SfM projects resulted in a single processing “block,” indicating that
¹⁴³ all images in the project were optimized and processed together.

¹⁴⁴ **Creating canopy height models**

¹⁴⁵ We classified each survey area’s dense point cloud into “ground” and “non-ground” points using a cloth
¹⁴⁶ simulation filter algorithm (Zhang et al. 2016) implemented in the **lidR** (Roussel et al. 2019) package. We
¹⁴⁷ rasterized the ground points using the **raster** package (Hijmans et al. 2019) to create a digital terrain model
¹⁴⁸ representing the ground underneath the vegetation at 1 meter resolution. We created a canopy height model
¹⁴⁹ by subtracting the digital terrain model from the digital surface model created in Pix4Dmapper.

¹⁵⁰ **Tree detection**

¹⁵¹ We tested a total of 7 automatic tree detection algorithms and a total of 177 parameter sets on the canopy
¹⁵² height model or the dense point cloud to locate trees within each site (Table XXXXX; algorithm, number of
¹⁵³ parameter sets, reference). We used 3 parameter sets of a variable window filter implemented in **ForestTools**
¹⁵⁴ (Plowright 2018) including the default variable window filter function in **ForestTools** as well as the “pines”
¹⁵⁵ and “combined” functions from Popescu and Wynne (2004). We used 6 parameter sets of a local maximum
¹⁵⁶ filter implemented in **lidR**. We used 131 parameter sets of the algorithm from Li et al. (2012), which operates
¹⁵⁷ on the original point cloud. These parameter sets included those from Shin et al. (2018) and Jakubowski et
¹⁵⁸ al. (2013). We used 3 parameter sets of the **watershed** algorithm implemented in **lidR**, which is a wrapper
¹⁵⁹ for a function in the **EBImage** package (Pau et al. 2010). We used 3 parameter sets of **ptrees** (Vega et al.
¹⁶⁰ 2014) implemented in **lidR** (Roussel et al. 2019) and **lidRplugins** (Roussel 2019) and which operates on
¹⁶¹ the raw point cloud, without first normalizing it to height above ground level (i.e.. subtracting the ground
¹⁶² elevation from the dense point cloud). We used the default parameter set of the **multichm** (Eysn et al. 2015)
¹⁶³ algorithm implemented in **lidR** (Roussel et al. 2019) and **lidRplugins** (Roussel 2019). We used 30 parameter
¹⁶⁴ sets of the experimental algorithm **lmfx** (Roussel 2019).

165 **Map ground data**

166 Each orthorectified reflectance map was inspected to locate the 5 orange “X”s marking the center of the
167 field plots. We were able to locate 110 out of 180 field plots and were then able to use these plots for
168 validation of automated tree detection algorithms. We used the `sf` package (Pebesma et al. 2019) to convert
169 distance-from-center and azimuth measurements of each tree in the ground plots to an x-y position on the
170 SfM-derived reflectance map using the x-y position of the orange X visible in the reflectance map as the
171 center.

172 **Correspondence of automatic tree detection with ground data**

173 We calculated 7 forest structure metrics for each field plot using the ground data collected by Fettig et al.
174 (2019): total number of trees, number of trees greater than 15 meters, number of trees less than 15 meters,
175 mean height of trees, 25th percentile tree height, 75th percentile tree height, mean distance to nearest tree
176 neighbor, mean distance to 2nd nearest neighbor.

177 For each tree detection algorithm and parameter set described above, we calculated the same set of 7 structure
178 metrics within the footprint of the validation field plots. We calculated the Pearson’s correlation and root
179 mean square error (RMSE) between the ground data and the aerial data for each of the 7 structure metrics
180 for each of the 177 automatic tree detection algorithms/parameter sets.

181 For each algorithm and parameter set, we calculated its performance relative to other algorithms as whether
182 its Pearson’s correlation was within 5% of the highest Pearson’s correlation as well as whether its RMSE was
183 within 5% of the lowest RMSE. For each algorithm/parameter set, we summed the number of forest structure
184 metrics for which it reached these 5% thresholds. For automatically detecting trees across the whole study,
185 we selected the algorithm/parameter set that performed well across the most number of forest metrics.

186 **Segmentation of crowns**

187 We delineated individual tree crowns with a marker controlled watershed segmentation algorithm (Meyer and
188 Beucher 1990) using the detected treetops as markers implemented in the `ForestTools` package (Plowright
189 2018). If the automatic segmentation algorithm failed to generate a crown segment for a detected tree (e.g.,
190 often snags with a very small crown footprint), a circular crown was generated with a radius of 0.5 meters. If
191 the segmentation generated multiple polygons for a single detected tree, only the polygon containing the
192 detected tree was retained. Image overlap decreases near the edges of the overall flight path, which reduces
193 the quality of the SfM processing in those areas. Thus, we excluded segmented crowns within 35 meters of
194 the edge of the survey area.

195 We used the `velox` package (Hunziker 2017) to extract all the pixel values from the orthorectified reflectance
196 map for each of the 5 narrow bands within each segmented crown polygon. Per pixel, we additionally
197 calculated the normalized difference vegetation index (NDVI; Rouse et al. (1973)), the normalized difference
198 red edge (NDRE; Gitelson and Merzlyak (1994)), the red-green index (RGI; Coops et al. (2006)), the red
199 edge chlorophyll index (CI[red edge]; Clevers and Gitelson (2013)), and the green chlorophyll index (CI[green];
200 Clevers and Gitelson (2013)). For each crown polygon, we calculated the mean value for each raw and derived
201 reflectance band (5 raw; 5 derived).

202 Classification of trees

203 We overlaid the segmented crowns on the reflectance maps from 20 sites spanning the latitudinal and
204 elevational gradient in the study. Using QGIS, we hand classified XXXX trees as live/dead and as one
205 of 5 dominant species in the study area (*Pinus ponderosa*, *Pinus lambertiana*, *Abies concolor*, *Calocedrus*
206 *decurrens*, or *Quercus kelloggii*) using the mapped ground data as a guide.

207 We used all 10 mean values of the reflectance bands for each tree crown polygon to predict whether the hand
208 classified trees were alive or dead using a boosted logistic regression model implemented in the `caret` package
209 (Kuhn 2008). For just the living trees, we similarly used all 10 reflectance values to predict the tree species
210 using regularized discriminant analysis implemented in the `caret` package, which proved to have the highest
211 accuracy for a training dataset (accuracy = XXXXX, kappa = XXXXX).

212 Finally, we used these models to classify all tree crowns in the data set as alive or dead as well as the species
213 of living trees.

214 Allometric scaling of height to basal area

215 We converted the height of each tree determined using the canopy height model to its basal area. Using
216 the tree height and diameter at breast height (DBH; breast height = 1.37m) ground data from Fettig et al.
217 (2019), we fit a simple linear regression to predict DBH from height for each of the 5 dominant species. Using
218 the model-classified tree species of each segmented tree, we used the corresponding linear relationship for
219 that species to estimate the DBH given the tree's height. We then calculated each tree's basal area, assuming
220 no tapering from breast height.

221 Note on assumptions about dead trees

222 For the purposes of this study, we assumed that all dead trees were ponderosa pine and were thus host trees.
223 This is a reasonably good assumption, given that Fettig et al. (2019) found that 73.4% of the dead trees in

224 the coincident ground plots were ponderosa pine.

225 **Rasterizing individual tree data**

226 Because the tree detection algorithms were validated against ground data at the plot level, we rasterized the
227 classified trees at a spatial resolution similar to that of the ground plots (rasterized to 20m x 20m equalling
228 400 m²; circular ground plots with 11.35m radius equalling 404 m²). In each raster cell, we tallied: number
229 of alive trees, number of dead trees, number of ponderosa pine trees, number of non-ponderosa pine trees,
230 basal area of ponderosa pine trees, basal area of non-ponderosa pine trees.

231 **Environmental data**

232 We used climatic water deficit (CWD) (Stephenson 1998) from the 1980-2010 mean value of the basin
233 characterization model (Flint et al. 2013) as an integrated measure of temperature and moisture conditions
234 for each cell. Higher values of CWD correspond to hotter, drier conditions and lower values correspond
235 to cooler, wetter conditions CWD has been shown to correlate well with broad patterns of tree mortality
236 in the Sierra Nevada (Young et al. 2017). We resampled the climatic water deficit product using bilinear
237 interpolation implemented in the `raster` package to match the 20m x 20m spatial scale of the other variables.
238 We converted the CWD value for each cell into a z-score representing that cell's deviation from the mean
239 CWD across the climatic range of Sierra Nevada ponderosa pine as determined from XXXXX herbarium
240 records described in Baldwin et al. (2017). Thus, a CWD z-score of one would indicate that the CWD at
241 that cell is one standard deviation hotter/drier than the mean CWD across all geolocated herbarium records
242 for ponderosa pine in the Sierra Nevada.

243 **Statistical model**

244 We used a generalized linear model with a zero-inflated binomial response and a logit link to predict the
245 probability of ponderosa pine mortality within each raster cell as a function of the crossed effects of ponderosa
246 pine quadratic mean diameter and density added to the crossed effect of overall quadratic mean diameter and
247 density as well as the interaction of each summand with climatic water deficit at each site.

248 To measure and account for spatial autocorrelation of the bark beetle behavioral processes underlying
249 ponderosa mortality, we first subsampled the data at each site to a random selection of 200, 20m x 20m
250 cells representing approximately 27.5% of the surveyed area. With these subsampled data, we included a
251 separate exact Gaussian process term per site of the interaction between the x- and y-position of each cell
252 using the `gp()` function in the `brms` package (Bürkner 2017). The Gaussian process accounts for spatial

253 autocorrelation in the model by jointly estimating the spatial covariance of the response variable with the
254 effects of the other covariates.

$$y_{i,j} \sim \begin{cases} 0, & p \\ Binom(n_i, \pi_i), & 1 - p \end{cases}$$
$$\text{logit}(\pi_i) = \beta_0 +$$
$$\beta_1 X_{cwd,j} +$$
$$\beta_1 X_{cwd,j} (\beta_2 X_{\text{pipoQMD},i} + \beta_3 X_{\text{pipoDensity},i} + \beta_4 X_{\text{pipoQMD},i} X_{\text{pipoDensity},i}) +$$
$$\beta_1 X_{cwd,j} (\beta_5 X_{\text{overallQMD},i} + \beta_6 X_{\text{overallDensity},i} + \beta_7 X_{\text{overallQMD},i} X_{\text{overallDensity},i}) +$$
$$\mathcal{GP}_j(x_i, y_i)$$

255 Where y_i is the number of dead trees in cell i , n_i is the sum of the dead trees and live ponderosa pine trees
256 in cell i , π_i is the probability of ponderosa pine tree mortality in cell i , p is the probability of there being
257 zero dead trees in a cell arising as a result of an unmodeled process, $X_{cwd,j}$ is the z-score of climatic water
258 deficit for site j , $X_{\text{pipoQMD},i}$ is the scaled quadratic mean diameter of ponderosa pine in cell i , $X_{\text{pipoDensity},i}$
259 is the scaled density of ponderosa pine trees in cell i , $X_{\text{overallQMD},i}$ is the scaled quadratic mean diameter
260 of all trees in cell i , $X_{\text{overallDensity},i}$ is the scaled density of all trees in cell i , x_i and y_i are the x- and y-
261 coordinates of the centroid of the cell in an EPSG3310 coordinate reference system, and \mathcal{GP}_j represents the
262 exact Gaussian process describing the spatial covariance between cells at site j .

263 We used 4 chains with 2000 iterations each (1000 warmup, 1000 samples), and confirmed chain convergence
264 by ensuring all `Rhat` values were less than 1.1 (Brooks and Gelman 1998). We used posterior predictive
265 checks to visually confirm model performance by overlaying the density curves of the predicted number of
266 dead trees per cell over the observed number (Gabry et al. 2019). For the posterior predictive checks, we
267 used 50 random samples from the model fit to generate 50 density curves and ensured curves were centered
268 on the observed distribution, paying special attention to model performance at capturing counts of zero.

269 Software and data availability

270 All data are available via the Open Science Framework. Statistical analyses were performed using the `brms`
271 packages. With the exception of the SfM software (Pix4Dmapper Cloud) and the GIS software QGIS, all
272 data carpentry and analyses were performed using R (R Core Team 2018).

273 Results

Table 2: Site characteristics for each of the 32 sites. The site name consists of the forest name, elevation band, and rep separated by an underscore. The Eldorado National Forest is ‘eldo’, the Stanislaus National Forest is ‘stan’, the Sierra National Forest is ‘sier’, and the Sequoia National Forest is ‘sequ’. The elevation band represents the lower bounds (in feet) of the 1000 foot elevation bands. Thus ‘3k’ implies that site was located between 3,000 and 4,000 feet. Aerially detected mortality and density of the whole site is presented along with the mortality and density calculated from the ground data (aerial / ground).

Site	CWD (mm)	CWD (z-score)	Survey area (ha)	Mortality (aerial/ground)	Density (tpha; aerial/ground)
eldo_3k_1	678.45	0.32	31.02	0.11/0.61	630.01/410.19
eldo_3k_2	706.48	0.50	30.61	0.12/0.36	444.26/647.42
eldo_3k_3	654.51	0.16	30.95	0.22/0.36	492.63/410.19
eldo_4k_1	570.43	-0.38	28.04	0.09/0.39	632.82/588.11
eldo_4k_2	642.20	0.08	28.41	0.15/0.78	338.20/271.82
eldo_5k_1	663.09	0.22	28.44	0.11/0.44	661.80/543.63
eldo_5k_2	627.38	-0.01	30.02	0.12/0.36	584.89/968.65
eldo_5k_3	598.66	-0.20	29.73	0.07/0.32	488.66/622.71
stan_3k_1	638.49	0.06	31.04	0.10/0.52	739.45/1037.84
stan_3k_2	739.23	0.71	18.78	0.40/0.78	433.53/405.25
stan_3k_3	761.64	0.86	30.10	0.22/0.41	558.43/326.18
stan_4k_1	540.16	-0.58	29.62	0.29/0.63	507.61/711.66
stan_4k_2	528.07	-0.66	30.54	0.18/0.56	481.85/256.99
stan_5k_1	523.51	-0.69	30.94	0.19/0.54	388.89/336.06
stan_5k_2	523.95	-0.68	29.94	0.21/0.44	399.33/622.71
sier_3k_1	763.54	0.87	30.42	0.19/0.48	651.46/850.04
sier_3k_2	767.64	0.90	30.05	0.20/0.77	438.84/153.21
sier_3k_3	772.98	0.93	29.77	0.32/0.77	511.26/459.62
sier_4k_1	841.25	1.38	30.43	0.54/0.51	576.15/538.69
sier_4k_2	764.38	0.88	29.30	0.33/0.57	499.43/854.98

Site	CWD (mm)	CWD (z-score)	Survey area (ha)	Mortality (aerial/ground)	Density (tpha; aerial/ground)
sier_4k_3	688.34	0.38	26.39	0.48/0.59	454.23/499.15
sier_5k_1	721.59	0.60	14.59	0.41/0.43	631.30/716.60
sier_5k_2	709.96	0.52	27.53	0.53/0.74	477.29/454.67
sier_5k_3	778.53	0.97	28.93	0.33/0.43	569.44/484.33
sequ_4k_1	766.61	0.89	29.59	0.50/0.56	365.81/607.88
sequ_4k_3	815.60	1.21	29.69	0.35/0.71	433.35/306.41
sequ_5k_1	718.24	0.58	27.12	0.35/0.52	364.01/444.79
sequ_5k_2	587.26	-0.27	29.10	0.45/0.43	478.31/499.15
sequ_5k_3	611.33	-0.12	31.34	0.42/0.48	348.68/494.21
sequ_6k_1	730.52	0.66	27.78	0.30/0.70	433.43/360.77
sequ_6k_2	689.51	0.39	11.83	0.26/0.43	699.04/934.06
sequ_6k_3	602.65	-0.17	26.51	0.36/0.32	535.54/691.89

274 Tree detection

275 We found that the experimental `lmfx` algorithm with parameter values of `dist2d = 1` and `ws = 2.5` (Roussel
 276 et al. 2019) performed the best across 7 measures of forest structure as measured by Pearson's correlation
 277 with ground data (Table 2).

Table 3: Correlation and differences between the best performing tree detection algorithm (`lmfx` with `dist2d = 1` and `ws = 2.5`) and the ground data. An asterisk next to the correlation or RMSE indicates that this value was within 5% of the value of the best-performing algorithm/parameter set.

Forest structure metric	Correlation with ground	RMSE	Mean error	Median error
height (m); 25th percentile	0.16	8.46	-2.30	-1.16
height (m); mean	0.29	7.81*	-3.43	-2.29
height (m); 75th percentile	0.35	10.33*	-4.85	-3.98
dist to 1st nearest neighbor (m)	0.55*	1.16*	0.13	0.26
dist to 2nd nearest neighbor (m)	0.61*	1.70*	0.08	0.12
dist to 3rd nearest neighbor (m)	0.50	2.29	0.17	0.19

Forest structure metric	Correlation with ground	RMSE	Mean error	Median error
total tree count	0.67*	8.68*	0.37	2.00
count of trees > 15m	0.43	7.38	1.18	0.00
count of trees < 15m	0.58	8.42	-0.66	2.00

278 Effect of local structure and regional climate on western pine beetle severity

279 We detected no main effect of climatic water deficit on the probability of ponderosa pine mortality within
280 each 20m x 20m cell.

281 We found a strong main effect of ponderosa pine local density, accounting for quadratic mean diameter of
282 ponderosa pine, with greater density increasing the probability of ponderosa pine mortality. Conversely,
283 we found a generally negative effect of quadratic mean diameter of ponderosa pine on the probability of
284 ponderosa mortality, suggesting that the western pine beetle attacked smaller trees, on average. There was a
285 strong positive interaction between the climatic water deficit and ponderosa pine quadratic mean diameter,
286 such that larger trees were more likely to increase the probability of ponderosa mortality in hotter, drier sites.

287 We found negative main effects of overall tree density and overall quadratic mean diameter. There was a
288 positive interaction between these variables, such that denser stands with larger trees did lead to greater
289 ponderosa pine mortality.

290 Spatial effects

291 We were able to calculate the length scale of the spatial autocorrelation in the probability of ponderosa
292 pine mortality at each site, accounting for forest structure and environmental factors. By fitting a separate
293 approximate Gaussian process for each site on the interacting variables of the x- and y- position, we measured
294 the spatial covariance inherent in the data, accounting for other factors. ## Discussion

295 Closer spacing between potential host trees facilitates dispersal

296 If this drives mortality patterns, then we'd expect the local density of ponderosa pine trees, accounting for
297 other variables, to have a strong positive effect.

298 Host preference for large trees

299 If this drives mortality patterns, then we'd expect the quadratic mean diameter of ponderosa pine trees,
300 accounting for other variables, to have a strong positive effect.

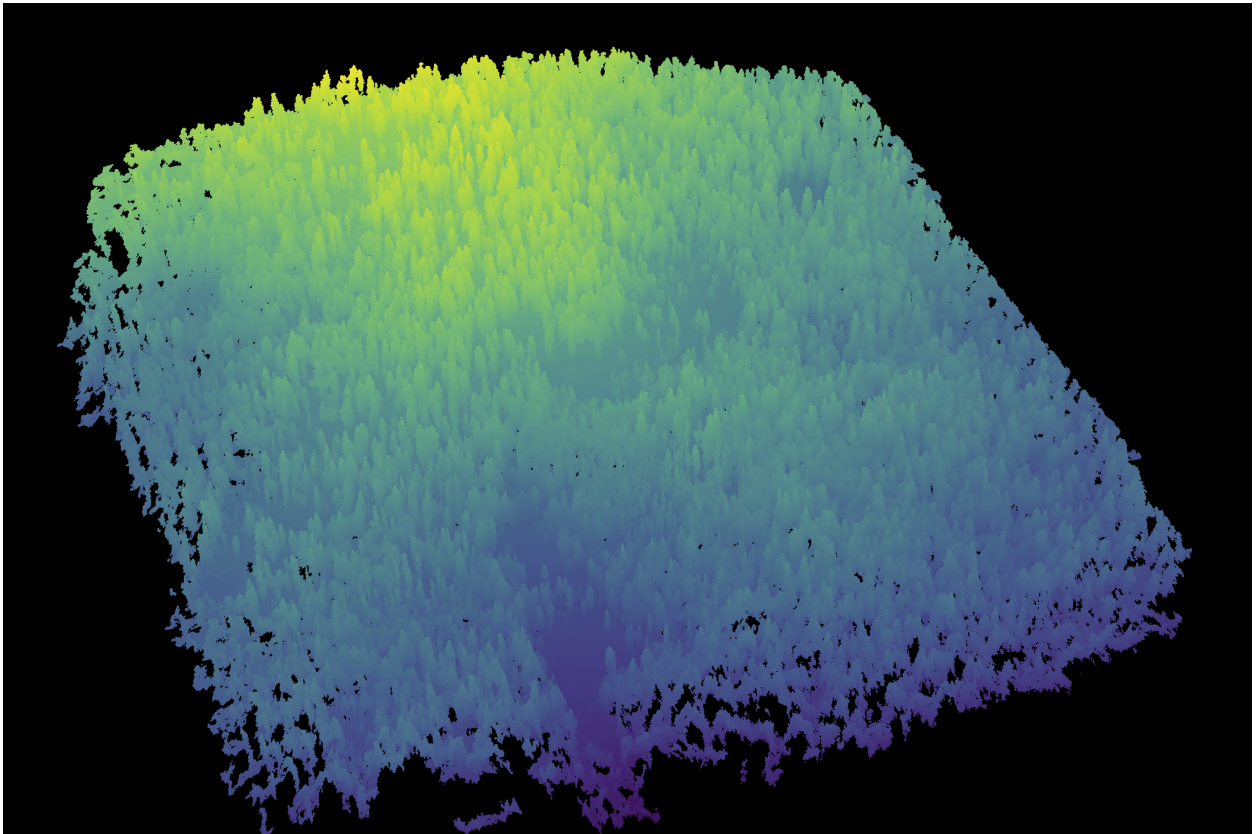


Figure 1: A dense point cloud representing ~40 hectares of forest is generated using Structure from Motion (SfM) processing of ~1900 images. The dense point cloud z- position represents the ground elevation plus the vegetation height.

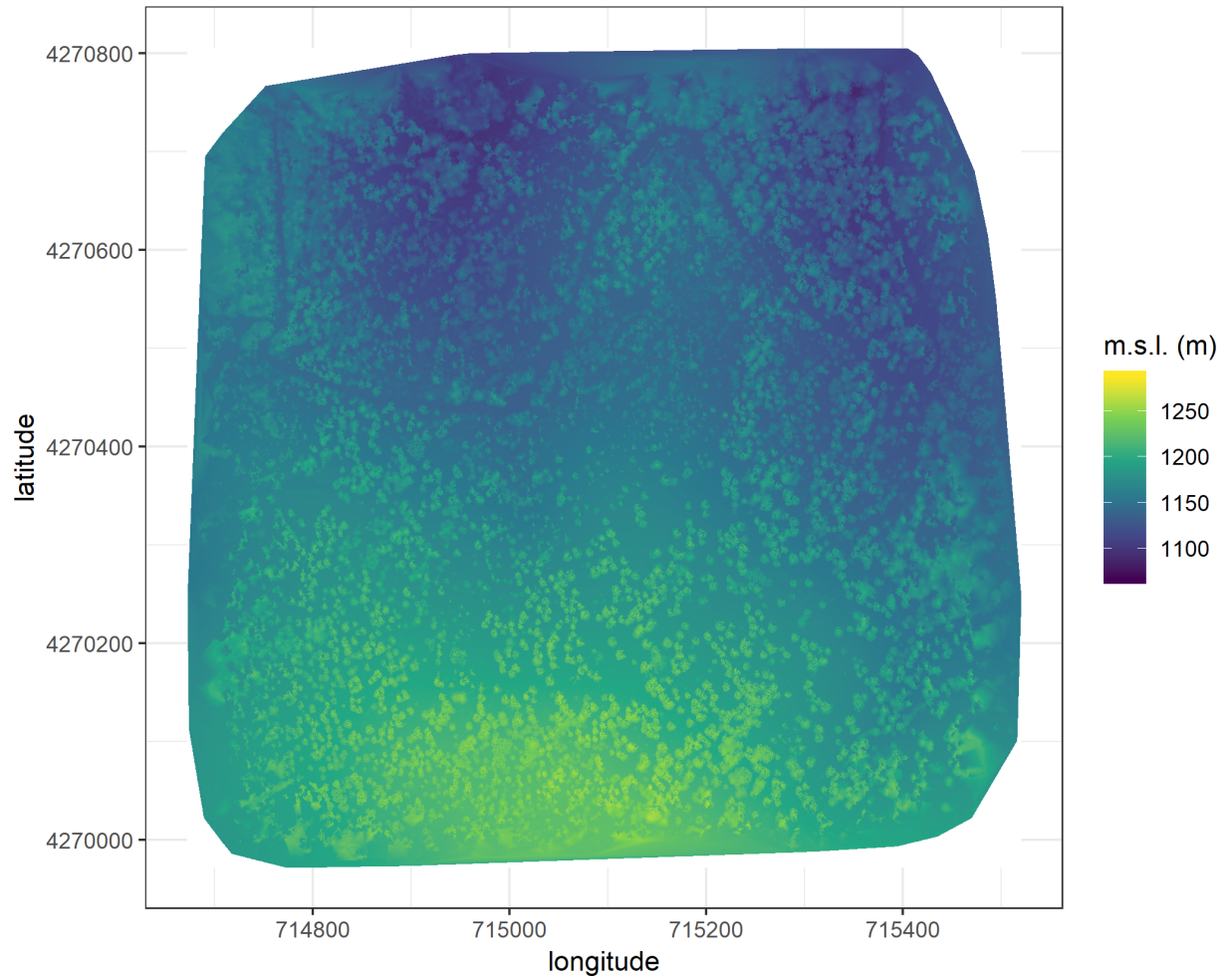


Figure 2: The digital surface model (DSM) is a 2-dimensional representation of the dense point cloud generated using structure from motion (SfM) processing. The DSM represents the ground elevation plus the vegetation height.

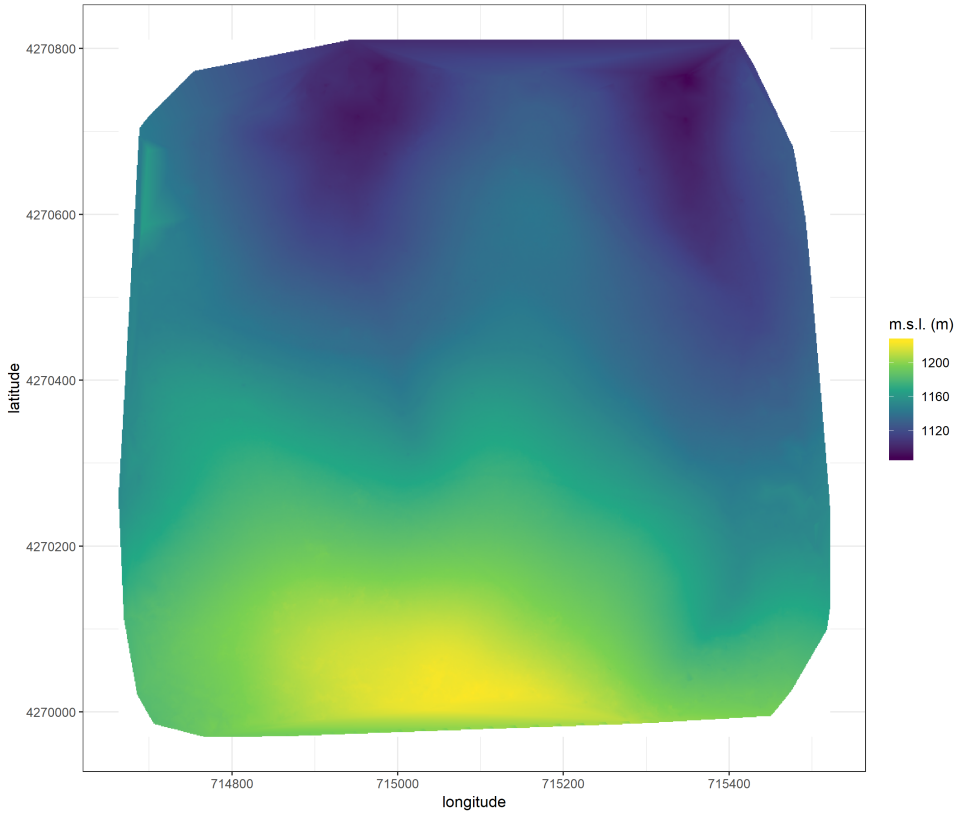


Figure 3: The digital terrain model (DTM) is generated by processing the dense point cloud using the cloth simulation filter algorithm (Zhang et al. 2016), which classifies points as “ground” or “not-ground” and then interpolates the “ground” elevation using Delaunay triangulation for the rest of the dense point cloud footprint. The DTM represents the ground elevation without any vegetation.

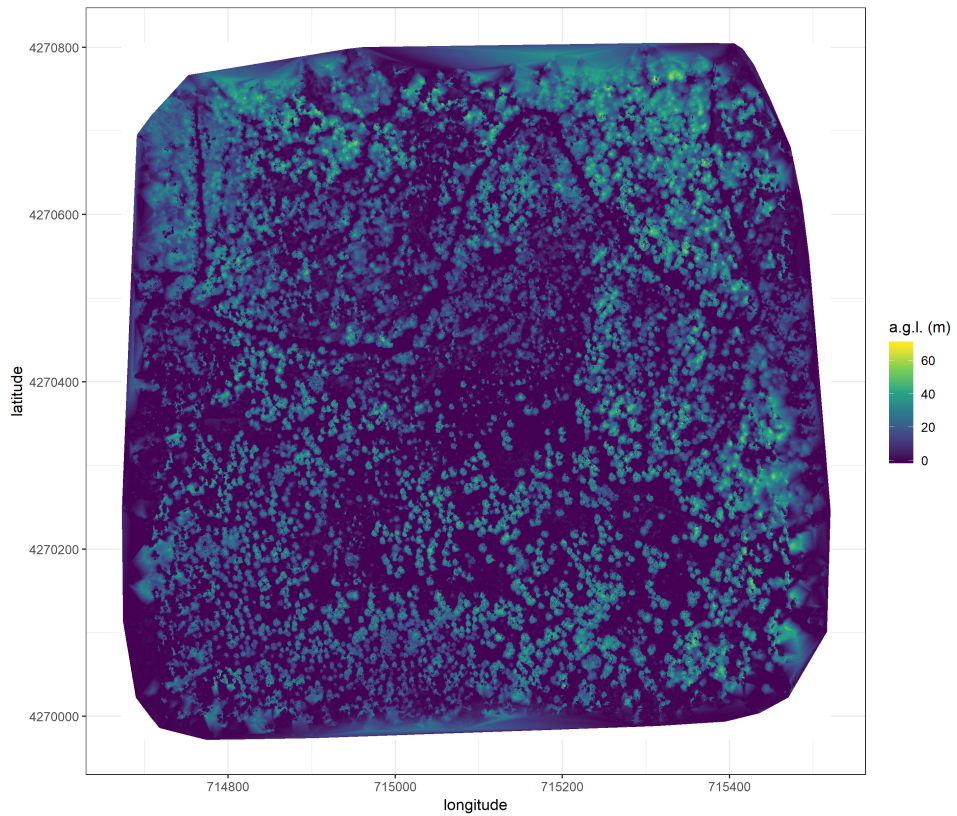


Figure 4: The canopy height model (CHM) is generated by subtracting the digital terrain model from the digital surface model. The CHM represents the height of all of the elevation above ground level.

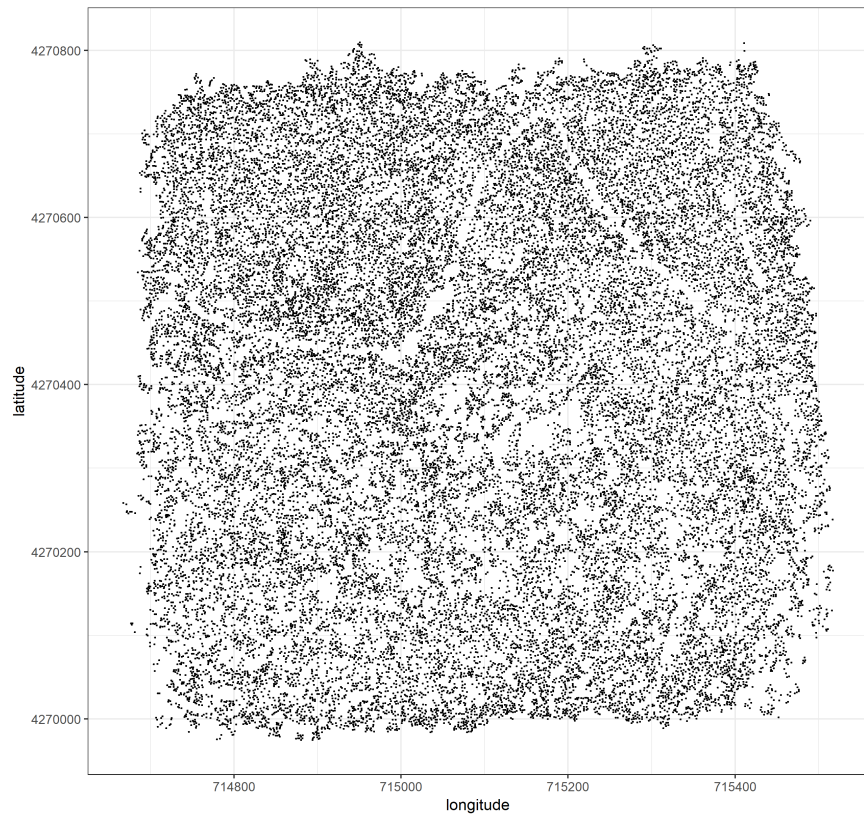


Figure 5: Tree locations are detected using the `lmfx` (Roussel et al. 2019) treetop detection algorithm on the dense point cloud.

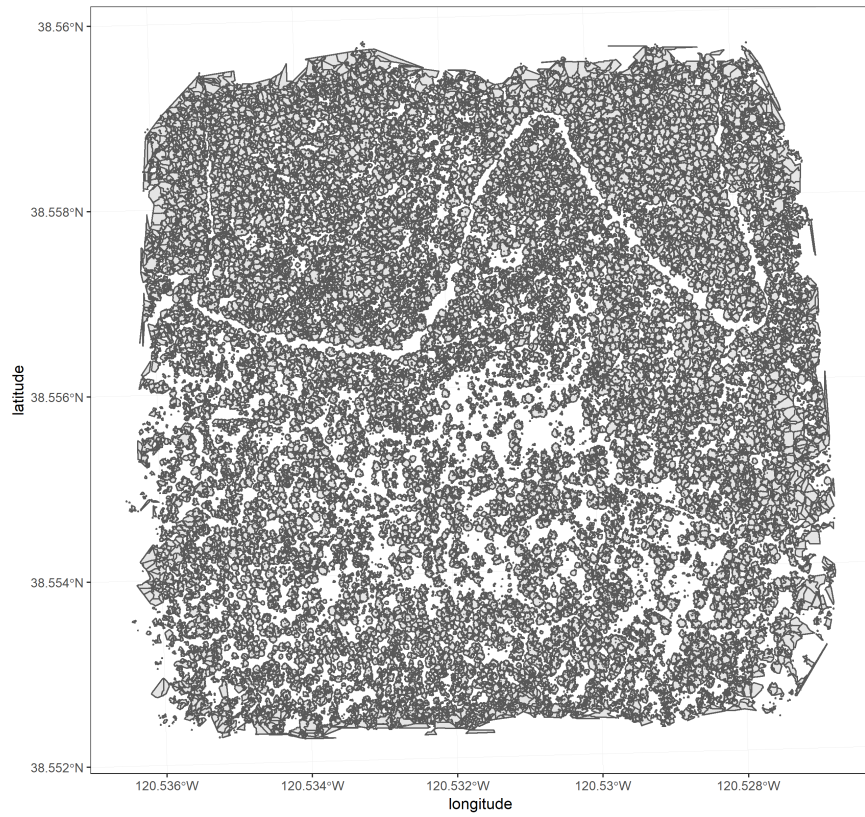


Figure 6: Individual crowns are delineated using a marker controlled watershed segmentation algorithm (Meyer and Beucher 1990, Plowright 2018) on the canopy height model (CHM) using the detected tree locations as a priority map. If the algorithm failed to delineate a crown for a tree that was identified in the tree detection step, a circular crown with a 0.5m buffer centered on point location of the detected tree was added as a crown. The crowns of snags were sometimes too small to be properly delineated, and the manually-created circular buffer

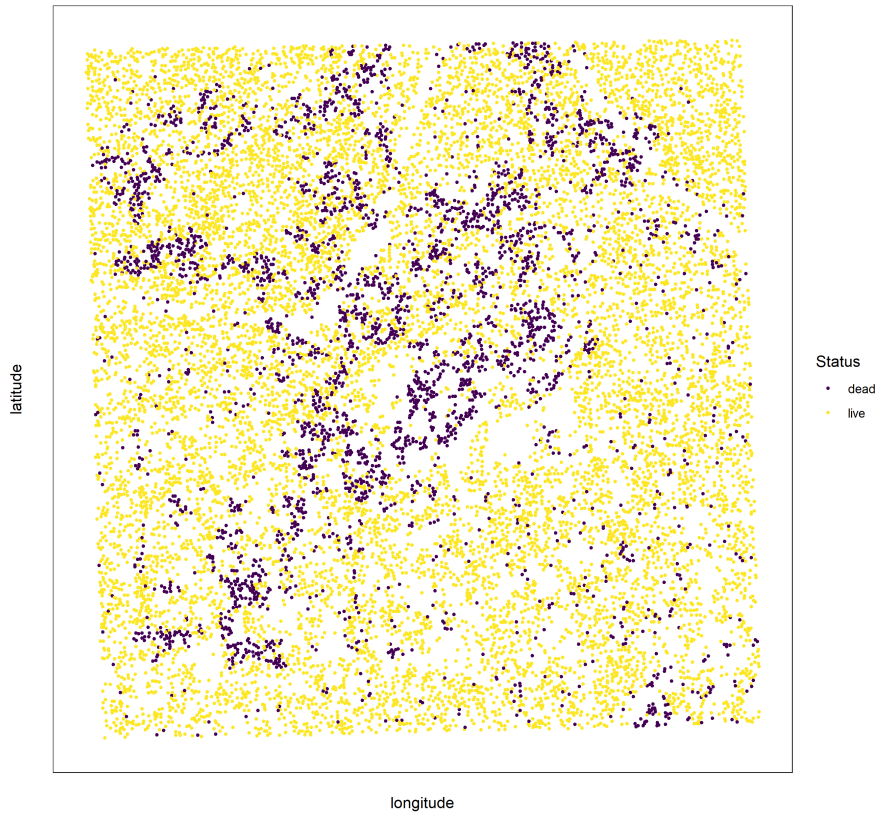


Figure 7: Each tree is classified as live or dead by extracting the pixel values from the 5 narrow bands of the Rededge3 camera (and 5 derived bands—see methods) in the orthomosaic within each segmented tree crown of the detected trees, taking their mean value, and using those means to predict live/dead status with a boosted logistic regression previously trained on a hand-classified set of segmented crowns from across the study area.

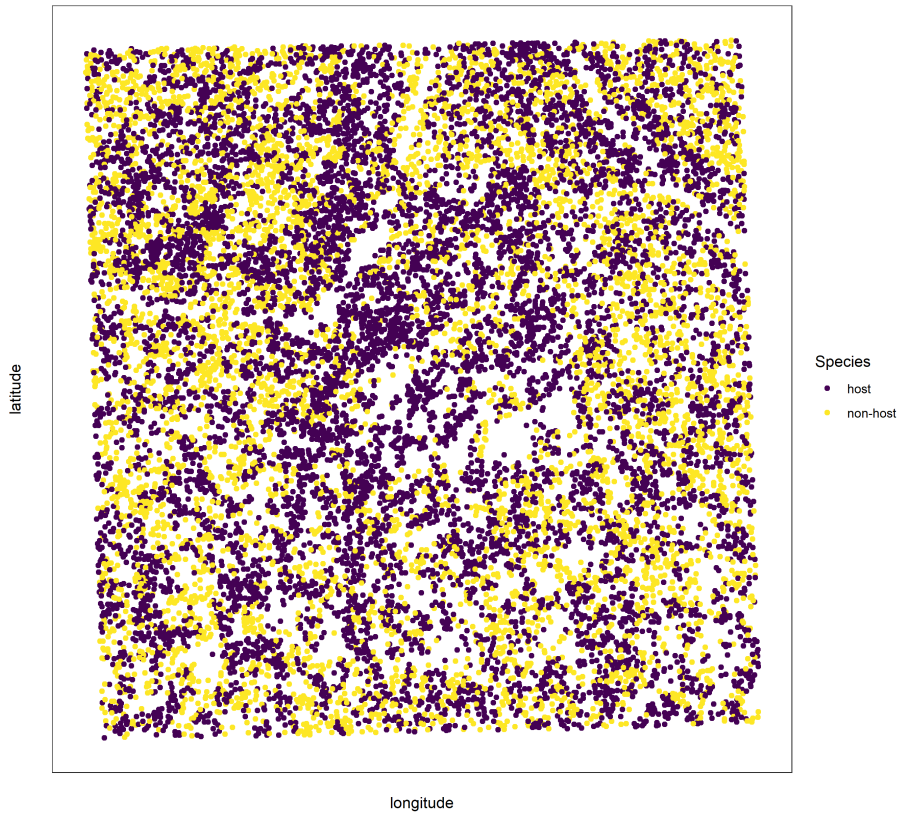


Figure 8: For each live tree, we classified its species using the same means of extracted pixel values across the 5 Rededge3 narrow bands (and 5 derived bands) as predictors in a regularized discriminant analysis previously trained on a hand-classified set of segmented crowns from across the study area.

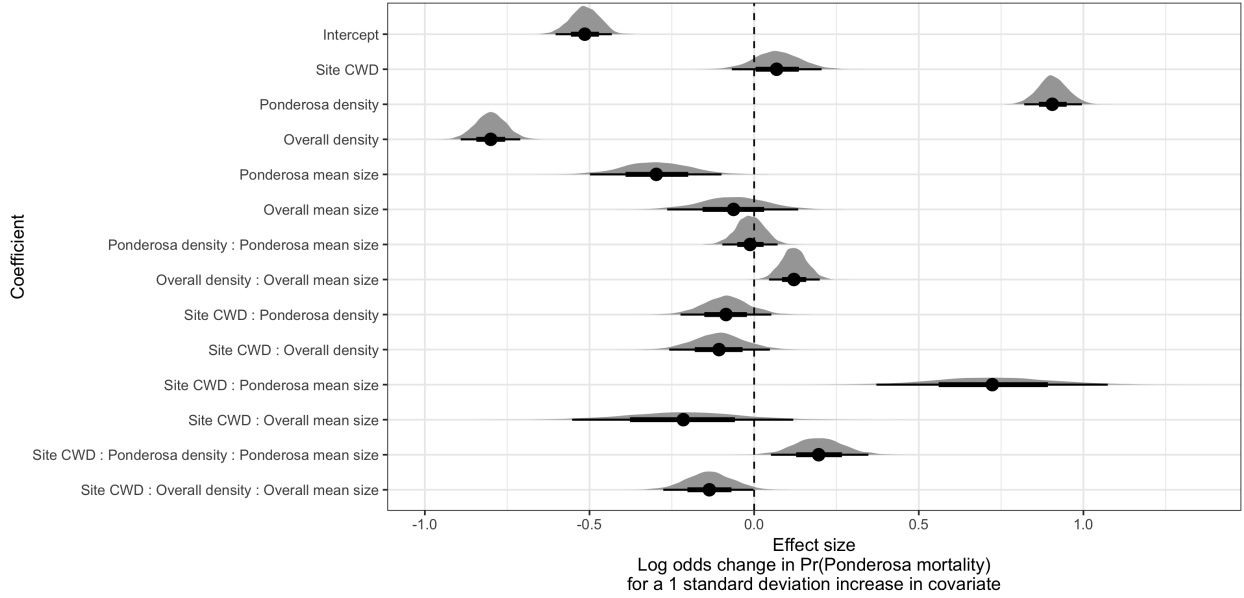


Figure 9: Posterior distributions of effect size from zero-inflated binomial model predicting the probability of ponderosa pine mortality in a 20m x 20m cell given forest structure characteristics of host trees and all trees within the cell, as well as a site-level climatic water deficit. The gray density distribution for each model covariate represents the density of the posterior distribution, the point underneath each density curve represents the median of the estimate, the bold interval surrounding the point estimate represents the 66% credible interval, and the thin interval surrounding the point estimate represents the 95% credible interval.

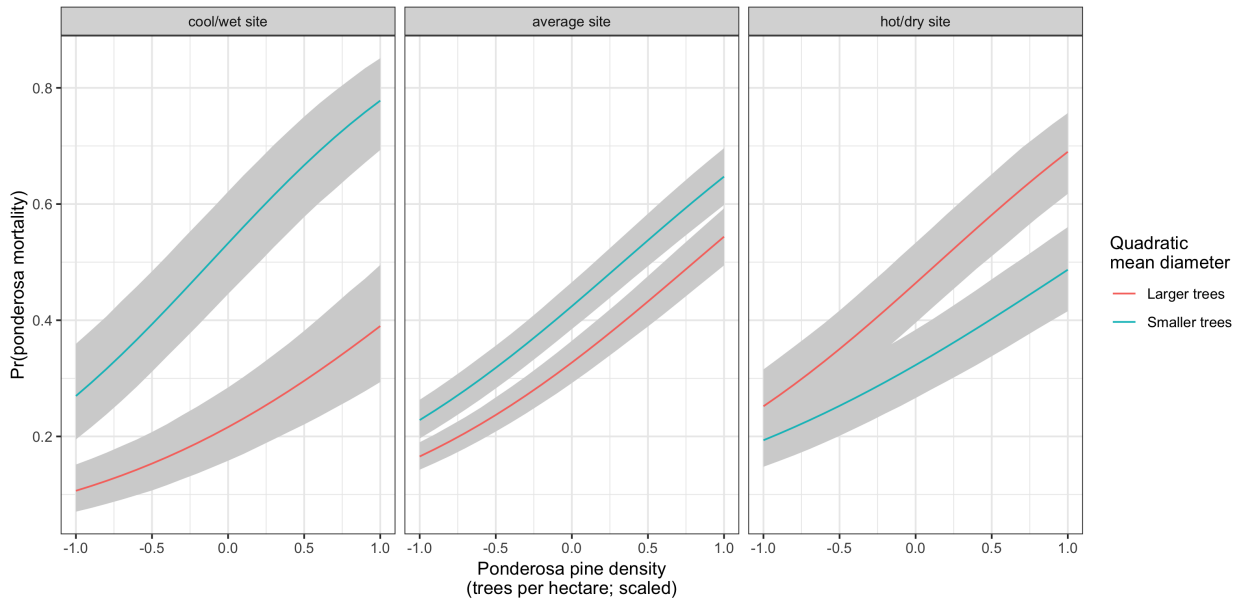


Figure 10: Line version of model results with 95% credible intervals showing primary influence of ponderosa pine structure on the probability of ponderosa pine mortality, and the interaction across climatic water deficit. The “larger trees” line represents the quadratic mean diameter of ponderosa pine 0.7 standard deviations above the mean, and the “smaller trees” line represents the quadratic mean diameter of ponderosa pine 0.7 standard deviations below the mean.

301 **Denser forests augment pheromone communication**

302 If this drives mortality patterns, then we'd expect the local density of all trees, accounting for other variables,
303 to have a strong positive effect.

304 **Tree crowding leads to greater average water stress per tree**

305 If this drives mortality patterns, then we'd expect the quadratic mean diameter of all trees, accounting for
306 other factors, to have a strong positive effect.

307 **Interaction between host density and host size**

308 A positive coefficient would indicate a combined effect of WPB preference for large trees and nearby host
309 availability.

310 **Interaction between all tree density and all tree size**

311 A positive coefficient would indicate a combined effect of tree crowding and pheromone communication
312 enhancement.

313 **Implications of forest structure/regional climate interactions**

314 We found that the probability of ponderosa pine mortality generally increased with local host availability
315 (host density), but also interacted with both host size and regional climate such that the role of tree size
316 became increasingly important in more climatically extreme sites. A smaller average tree size led to a lower
317 probability of ponderosa mortality in cool/wet sites and a larger average tree size led to a greater probability
318 of ponderosa mortality in hot/dry sites. These mortality patterns highlight a possible distinction in behavior
319 between the recent western bark beetle activity across the gradient of climatic water deficit. Even in the most
320 highly impacted forest stands (because our study sites were selected conditional on there being high levels of
321 western pine beetle activity), there is still a detectable effect of tree size such that the smaller (presumably
322 weaker) trees are getting killed in cooler/wetter sites, and the larger (presumably more well-defended) trees
323 are getting killed more in the hotter/drier sites. So while mortality is high everywhere, there does appear to
324 be a difference in the beetle choosiness across the climatic water deficit gradient.

325 **Similarities and differences with Fettig et al. (2019)**

326 Fettig et al. (2019) found positive relationship between number of trees killed and: total number of trees,
327 total basal area, stand density index.

328 Fettig et al. (2019) found negative relationship between the proportion of trees killed and: total number of
329 trees, stand density index.

330 Hayes et al. (2009) and Fettig et al. (2019) found measures of host availability explained less variation in
331 mortality than measures of stand density.

332 Negráñ et al. (2009) reported positive association of probability of ponderosa pine mortality and tree density
333 during a drought in Arizona.

334 Effect of competition may be masked because drought was so extreme Fettig et al. (2019); Floyd et al.
335 (2009), which is perhaps why we saw a counter-intuitive signal of increasing total basal area leading to lower
336 probability of ponderosa pine mortality.

337 **Broader context around field plots**

338 We surveyed 9 square kilometers of forest representing ~450,000 trees along a broad gradient. Site selection
339 and small plot size can influence inference. For instance, Fettig et al. (2019) reported statistically undetectable
340 differences in overall mortality in their plot network across 4 national forests. By expanding the hectarage
341 surveyed by a factor of 200, we detected dramatic differences in overall mortality.

342 This is about more than sample size (though that helps). This is also about capturing the local disturbance
343 phenomenon.

344 **Implications for future forest structure**

345 We have demonstrated that forest structure (local host density and size) affected the cumulative severity
346 of the western pine beetle in the Sierra Nevada in the 2012 to 2015 drought and its aftermath. Clearly,
347 this forest insect disturbance has reciprically impacted the forest structure, with uncertain consequences for
348 long-term forest dynamics.

349 Small trees are getting killed in cooler/wetter sites, larger trees getting killed in hotter/drier sites. Perhaps
350 the cooler/wetter sites are resisting even this massive disturbance event?

351 **Spatial effect**

352 The western pine beetle is known to exhibit strong aggregation and anti-aggregation behavior arising from
353 its pheromone communication, and thus it is likely that the measured spatial covariance in this study is
354 attributable in part to the magnitude of this effect at each site.

355 Some studies have suggested that “outbreak” conditions are distinguishable by clustered tree mortality, but
356 this is perhaps challenging to tease apart (Raffa et al. 2008). Our modeling framework allows for a joint
357 estimation of the effects of forest structure, environmental condition, and the spatial effect. This framework
358 would be enhanced with confidence in individual tree level data, and a lot of it, along with a strong gradient
359 of environmental conditions and forest structure.

360 We won’t interpret this measure of contagion, because the uncertainties in this particular study are too great
361 (tree detection, species classification, dead trees all assumed to be WPB hosts, didn’t account for topographic
362 effects which could also manifest as part of this spatial covariance process). We do suggest that this could be
363 a meaningful and quantifiable means of assessing bark beetle “stage of outbreak”.

364 **Future spatial directions (will cut this; here for now so I can write it down elsewhere)**

365 Perhaps could also compare relative effect of individual tree spacing (Voronoi polygon area) with the length
366 scale parameter at a certain site to get at a similar question. A big voronoi polygon area effect and a short
367 covariance kernel tells us that it’s a water stress effect– a crowded tree gets attacked regardless of whether
368 nearby trees were attacked. A small voronoi polygon area effect and a long covariance kernel tells us that the
369 mortality is patterned more based on there being spillover from nearby attacked neighbors instead of how
370 crowded any given tree is. I expect we might see different relative magnitudes of voronoi polygon area and
371 covariance kerel effects depending on CWD.

372 **Important considerations**

373 Cumulative effect of elevated insect activity, as mortality was spread out over 5 years and we surveyed at the
374 end. All the detected dead trees were considered ponderosa pine– we know this is wrong. Only about 3 out
375 of 4 dead trees in Fettig et al. (2019) were ponderosa.

376 **Room for improvement**

- 377 • Better geometry by using higher overlap, more spatially resolved images.
- 378 • Better image classification and scalability by using instrumentation having spectral overlap with more
379 widely deployed instrumentation (e.g., Landsat).
- 380 • Better tree detection using machine learning approaches
- 381 • Our live/dead classifier works pretty well.
- 382 • Our species classifier could improve. Perhaps also using machine learning approaches.

383 (Seidl et al. 2015) (Preisler et al. 2017)

384 **References**

- 385 Baldwin, B. G., A. H. Thornhill, W. A. Freyman, D. D. Ackerly, M. M. Kling, N. Morueta-Holme, and B. D.
386 Mishler. 2017. Species richness and endemism in the native flora of California. *American Journal of Botany*
387 104:487–501.
- 388 Brooks, S. P., and A. Gelman. 1998. General Methods for Monitoring Convergence of Iterative Simulations.
389 *Journal of Computational and Graphical Statistics* 7:434.
- 390 Bürkner, P.-C. 2017. **Brms** : An *R* Package for Bayesian Multilevel Models Using *Stan*. *Journal of Statistical*
391 *Software* 80.
- 392 Clevers, J., and A. Gitelson. 2013. Remote estimation of crop and grass chlorophyll and nitrogen content using
393 red-edge bands on Sentinel-2 and -3. *International Journal of Applied Earth Observation and Geoinformation*
394 23:344–351.
- 395 Coops, N. C., M. Johnson, M. A. Wulder, and J. C. White. 2006. Assessment of QuickBird high spatial
396 resolution imagery to detect red attack damage due to mountain pine beetle infestation. *Remote Sensing of*
397 *Environment* 103:67–80.
- 398 DJI. 2015a. Zenmuse X3 - Creativity Unleashed. <https://www.dji.com/zenmuse-x3/info>.
- 399 DJI. 2015b. DJI - The World Leader in Camera Drones/Quadcopters for Aerial Photography. <https://www.dji.com/matrice100/info>.
- 400 Easy, D. M. 2018. Map Pilot for DJI. <https://itunes.apple.com/us/app/map-pilot-for-dji/id1014765000?mt=8>.
- 401 Eysn, L., M. Hollaus, E. Lindberg, F. Berger, J.-M. Monnet, M. Dalponte, M. Kobal, M. Pellegrini, E.
402 Lingua, D. Mongus, and N. Pfeifer. 2015. A Benchmark of Lidar-Based Single Tree Detection Methods Using
403 Heterogeneous Forest Data from the Alpine Space. *Forests* 6:1721–1747.
- 404 Farr, T. G., P. A. Rosen, E. Caro, R. Crippen, R. Duren, S. Hensley, M. Kobrick, M. Paller, E. Rodriguez, L.
405 Roth, D. Seal, S. Shaffer, J. Shimada, J. Umland, M. Werner, M. Oskin, D. Burbank, and D. Alsdorf. 2007.
406 The Shuttle Radar Topography Mission. *Reviews of Geophysics* 45.
- 407 Fettig, C. J. 2012. Chapter 2: Forest health and bark beetles. *in* Managing Sierra Nevada Forests. PSW-
408 GTR-237. USDA Forest Service.
- 409 Fettig, C. J., L. A. Mortenson, B. M. Bulaon, and P. B. Foulk. 2019. Tree mortality following drought in the
410 central and southern Sierra Nevada, California, U.S. *Forest Ecology and Management* 432:164–178.
- 411 Flint, L. E., A. L. Flint, J. H. Thorne, and R. Boynton. 2013. Fine-scale hydrologic modeling for regional land-

- 413 scape applications: The California Basin Characterization Model development and performance. Ecological
414 Processes 2:25.
- 415 Floyd, M. L., M. Clifford, N. S. Cobb, D. Hanna, R. Delph, P. Ford, and D. Turner. 2009. Relationship of
416 stand characteristics to drought-induced mortality in three Southwestern piñonJuniper woodlands. Ecological
417 Applications 19:1223–1230.
- 418 Gabry, J., D. Simpson, A. Vehtari, M. Betancourt, and A. Gelman. 2019. Visualization in Bayesian workflow.
419 Journal of the Royal Statistical Society: Series A (Statistics in Society) 182:389–402.
- 420 Gitelson, A., and M. N. Merzlyak. 1994. Spectral Reflectance Changes Associated with Autumn Senescence
421 of *Aesculus hippocastanum* L. and *Acer platanoides* L. Leaves. Spectral Features and Relation to Chlorophyll
422 Estimation. Journal of Plant Physiology 143:286–292.
- 423 Hayes, C. J., C. J. Fettig, and L. D. Merrill. 2009. Evaluation of Multiple Funnel Traps and Stand
424 Characteristics for Estimating Western Pine Beetle-Caused Tree Mortality. Journal of Economic Entomology
425 102:2170–2182.
- 426 Hijmans, R. J., J. van Etten, M. Sumner, J. Cheng, A. Bevan, R. Bivand, L. Busetto, M. Canty, D. Forrest,
427 A. Ghosh, D. Golicher, J. Gray, J. A. Greenberg, P. Hiemstra, I. for M. A. Geosciences, C. Karney, M.
428 Mattiuzzi, S. Mosher, J. Nowosad, E. Pebesma, O. P. Lamigueiro, E. B. Racine, B. Rowlingson, A. Shortridge,
429 B. Venables, and R. Wueest. 2019. Raster: Geographic Data Analysis and Modeling.
- 430 Hunziker, P. 2017. Velox: Fast Raster Manipulation and Extraction.
- 431 Jakubowski, M. K., W. Li, Q. Guo, and M. Kelly. 2013. Delineating Individual Trees from Lidar Data: A
432 Comparison of Vector- and Raster-based Segmentation Approaches. Remote Sensing 5:4163–4186.
- 433 Kane, V. R., M. P. North, J. A. Lutz, D. J. Churchill, S. L. Roberts, D. F. Smith, R. J. McGaughey, J. T.
434 Kane, and M. L. Brooks. 2014. Assessing fire effects on forest spatial structure using a fusion of Landsat and
435 airborne LiDAR data in Yosemite National Park. Remote Sensing of Environment 151:89–101.
- 436 Kuhn, M. 2008. Building Predictive Models in R Using the caret Package. Journal of Statistical Software
437 28:1–26.
- 438 Larson, A. J., and D. Churchill. 2012. Tree spatial patterns in fire-frequent forests of western North America,
439 including mechanisms of pattern formation and implications for designing fuel reduction and restoration
440 treatments. Forest Ecology and Management 267:74–92.
- 441 Li, W., Q. Guo, M. K. Jakubowski, and M. Kelly. 2012. A New Method for Segmenting Individual Trees

- 442 from the Lidar Point Cloud. *Photogrammetric Engineering & Remote Sensing* 78:75–84.
- 443 Meyer, F., and S. Beucher. 1990. Morphological segmentation. *Journal of Visual Communication and Image*
- 444 *Representation* 1:21–46.
- 445 Micasense. 2015. MicaSense. <https://support.micasense.com/hc/en-us/articles/215261448-RedEdge-User-Manual-PDF-Download>
- 446 Millar, C. I., and N. L. Stephenson. 2015. Temperate forest health in an era of emerging megadisturbance.
- 447 *Science* 349:823–826.
- 448 Morris, J. L., S. Cottrell, C. J. Fettig, W. D. Hansen, R. L. Sherriff, V. A. Carter, J. L. Clear, J. Clement, R.
- 449 J. DeRose, J. A. Hicke, P. E. Higuera, K. M. Mattor, A. W. R. Seddon, H. T. Seppä, J. D. Stednick, and S.
- 450 J. Seybold. 2017. Managing bark beetle impacts on ecosystems and society: Priority questions to motivate
- 451 future research. *Journal of Applied Ecology* 54:750–760.
- 452 Negrón, J. F., J. D. McMillin, J. A. Anhold, and D. Coulson. 2009. Bark beetle-caused mortality in a
- 453 drought-affected ponderosa pine landscape in Arizona, USA. *Forest Ecology and Management* 257:1353–1362.
- 454 North, M. P., S. L. Stephens, B. M. Collins, J. K. Agee, G. Aplet, J. F. Franklin, and P. Z. Fule. 2015.
- 455 Reform forest fire management. *Science* 349:1280–1281.
- 456 Pau, G., F. Fuchs, O. Sklyar, M. Boutros, and W. Huber. 2010. EBImagean R package for image processing
- 457 with applications to cellular phenotypes. *Bioinformatics* 26:979–981.
- 458 Pebesma, E., R. Bivand, E. Racine, M. Sumner, I. Cook, T. Keitt, R. Lovelace, H. Wickham, J. Ooms, K.
- 459 Müller, and T. L. Pedersen. 2019. Sf: Simple Features for R.
- 460 Plowright, A. 2018. ForestTools: Analyzing Remotely Sensed Forest Data.
- 461 Popescu, S. C., and R. H. Wynne. 2004. Seeing the Trees in the Forest: Using Lidar and Multispectral Data
- 462 Fusion with Local Filtering and Variable Window Size for Estimating Tree Height. *PHOTOGGRAMMETRIC*
- 463 *ENGINEERING*:16.
- 464 Preisler, H. K., N. E. Grulke, Z. Heath, and S. L. Smith. 2017. Analysis and out-year forecast of beetle,
- 465 borer, and drought-induced tree mortality in California. *Forest Ecology and Management*. 399: 166–178
- 466 399:166–178.
- 467 R Core Team. 2018. R: A Language and Environment for Statistical Computing. R Foundation for Statistical
- 468 Computing, Vienna, Austria.
- 469 Raffa, K. F., B. H. Aukema, B. J. Bentz, A. L. Carroll, J. A. Hicke, M. G. Turner, and W. H. Romme. 2008.
- 470 Cross-scale Drivers of Natural Disturbances Prone to Anthropogenic Amplification: The Dynamics of Bark

- 471 Beetle Eruptions. BioScience 58:501–517.
- 472 Raffa, K. F., J.-C. Grégoire, and B. Staffan Lindgren. 2015. Natural History and Ecology of Bark Beetles.
- 473 Pages 1–40 in Bark Beetles. Elsevier.
- 474 Rouse, W., R. H. Haas, W. Deering, and J. A. Schell. 1973. MONITORING THE VERNAL ADVANCEMENT
- 475 AND RETROGRADATION (GREEN WAVE EFFECT) OF NATURAL VEGETATION. Type II Report,
- 476 Goddard Space Flight Center, Greenbelt, MD, USA.
- 477 Roussel, J.-R. 2019. lidRplugins: Extra functions and algorithms for lidR package.
- 478 Roussel, J.-R., D. A. (. the documentation), F. D. B. (. bugs and improved catalog features), and A. S. M. (.
- 479 lassnags). 2019. lidR: Airborne LiDAR Data Manipulation and Visualization for Forestry Applications.
- 480 Seidl, R., J. Müller, T. Hothorn, C. Bässler, M. Heurich, and M. Kautz. 2015. Small beetle, large-scale
- 481 drivers: How regional and landscape factors affect outbreaks of the European spruce bark beetle. The Journal
- 482 of applied ecology 53:530–540.
- 483 Shin, P., T. Sankey, M. Moore, and A. Thode. 2018. Evaluating Unmanned Aerial Vehicle Images for
- 484 Estimating Forest Canopy Fuels in a Ponderosa Pine Stand. Remote Sensing 10:1266.
- 485 Stephenson, N. 1998. Actual evapotranspiration and deficit: Biologically meaningful correlates of vegetation
- 486 distribution across spatial scales. Journal of Biogeography 25:855–870.
- 487 USDAFS. 2019, February 11. Press Release: Survey finds 18 million trees died in California in 2018.
- 488 https://www.fs.usda.gov/Internet/FSE_DOCUMENTS/FSEPRD609321.pdf.
- 489 Vega, C., A. Hamrouni, S. El Mokhtari, J. Morel, J. Bock, J. P. Renaud, M. Bouvier, and S. Durrieu. 2014.
- 490 PTrees: A point-based approach to forest tree extraction from lidar data. International Journal of Applied
- 491 Earth Observation and Geoinformation 33:98–108.
- 492 Young, D. J. N., J. T. Stevens, J. M. Earles, J. Moore, A. Ellis, A. L. Jirka, and A. M. Latimer. 2017.
- 493 Long-term climate and competition explain forest mortality patterns under extreme drought. Ecology Letters
- 494 20:78–86.
- 495 Zhang, W., J. Qi, P. Wan, H. Wang, D. Xie, X. Wang, and G. Yan. 2016. An Easy-to-Use Airborne LiDAR
- 496 Data Filtering Method Based on Cloth Simulation. Remote Sensing 8:501.